Supporting Information for

Multiple coupling in plasmonic metal/dielectric hollow nanocavity arrays for high sensitive detection†

Jun Yin,[a] Yashu Zang,[a,b] Chuang Yue,[a,b] Xu He,[a,b] Hongtao Yang,[c] De-Yin Wu,[c] Min Wu,[d] Junyong Kang,[b] Zhihao Wu[e]* and Jing Li[a]*

[a.] *Pen-Tung Sah Institute of Micro-Nano Science and Technology, Xiamen University, Xiamen, 361005, China. E-mail: lijing@xmu.edu.cn;* [b.] *Department of Physics, Xiamen University, Xiamen, 361005, China;* [c.] *College of Chemistry and Chemical Engineering, Xiamen University, Xiamen, 361005, China;* [d.] *Xiamen Entry-Exit Inspection and Quarantine Bureau, Xiamen, 361026, China;* [e.] *Wuhan National Laboratory for Optoelectronics, School of Optical and Electronic Information, Huazhong University of Science and Technology, Wuhan, 430074, China. E-mail: zhihao.wu@hust.edu.cn*

## S1. Fabrication processes of Ag/ZnO HNS arrays
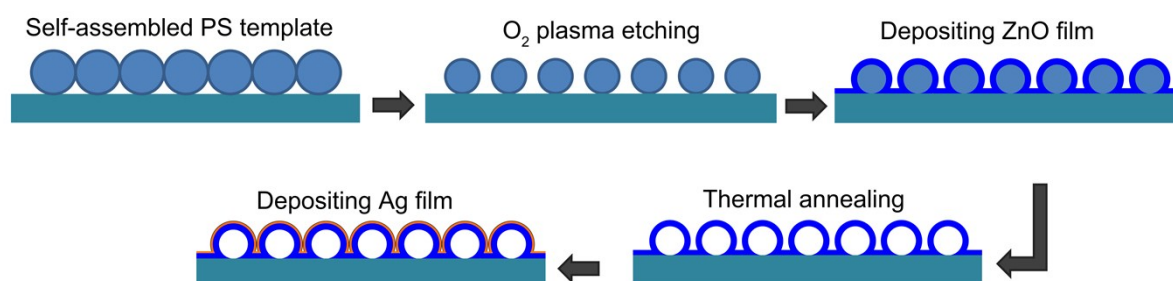
Figure S1. The fabrication processes of Ag/ZnO HNS arrays are schematically shown in figure by using the colloidal template method combined with the film deposition process.

The Ag/ZnO double-shell HNS periodic arrays were fabricated using the self-assembled PS nanospheres as template combined with the magnetron sputtering technology. Commercial PS nanospheres purchased from Thermo Scientific with the diameter of 500 nm were used as template materials to fabricate the double-shell HNS arrays. The fabrication processes are schematically shown in Figure S1 by using the colloidal template method[1] as described in our previous work.[2] In brief, firstly, spin-coating method was employed to self-

assemble monolayer PS nanospheres both on silicon and sapphire substrates with a hydrophilic surface. Reactive-ion etching (RIE) for different durations was introduced to adjust the size and distribution of the PS template. Then, ZnO film was deposited on the substrates using magnetron sputtering method followed by a thermal annealing process to form ZnO HNS arrays with an improved crystal quality. Finally, another Ag film depositing process proceeded to produce the double-shell Ag/ZnO hollow structure.

S2. WGM resonance in the ZnO HNS cavity
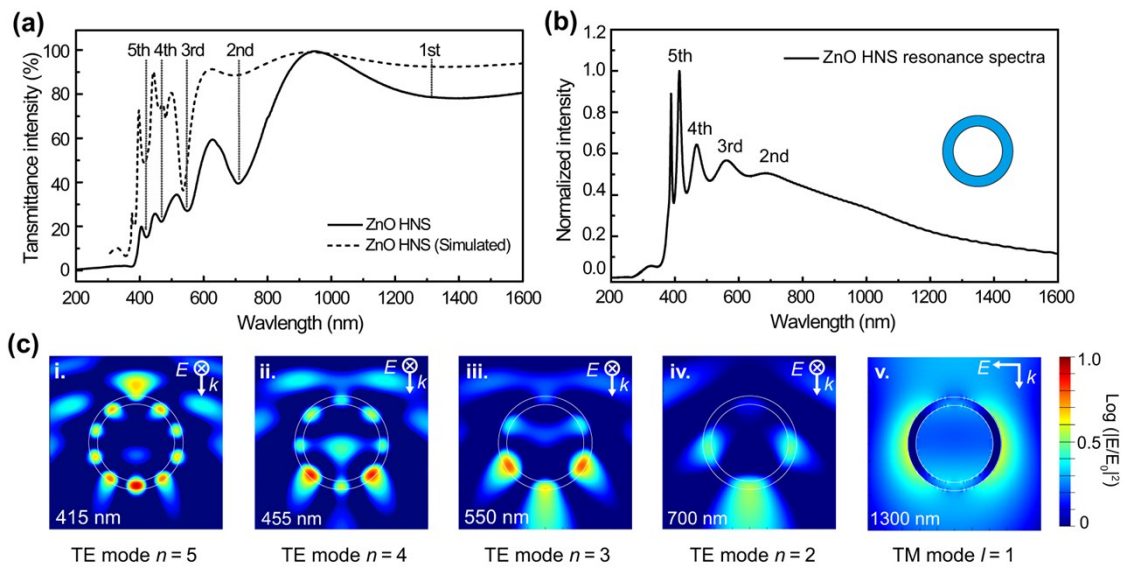
Figure S2. (a) Experimental (solid line) and simulated (dash line) transmission spectra of the ZnO HNS arrays on sapphire substrate. (b) Simulated resonance spectra in ZnO HNS nanocavity (Core diameter of 450 nm and shell thickness of 45 nm). (c) The simulated near field distribution patterns (i-v) under each resonance wavelength as in (b): the resonance peaks (415 nm, 455 nm, 550 nm and 700 nm) in the ZnO HNS cavity was identified as series of TE-mode WGM resonances as subscribed in the figure. As for the dip at ~1300 nm in the experimental transmission spectra, due to the much larger wavelength than the size of the ZnO HNS, the order of resonance seems much like Mie dipole resonance and in a TM mode (l = 1) as evidenced by the near-field pattern shown in v.

**S3. Plasmonic coupled WGM resonance in the Ag/ZnO HNS cavity**
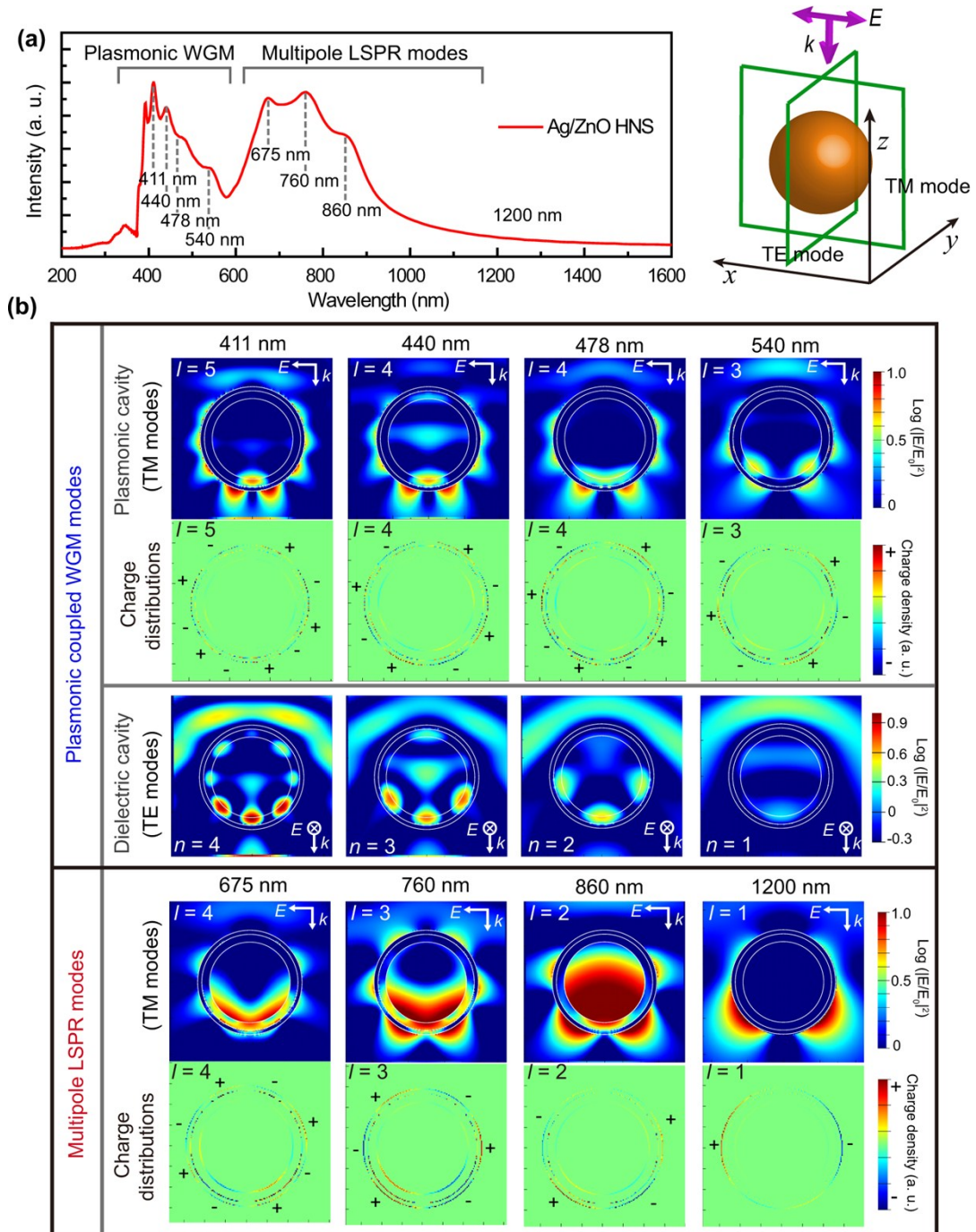
Figure S3. (a) Simulated resonance spectra in a single Ag/ZnO HNS nanocavity (core diameter of 450 nm, shell thickness of 45 nm in ZnO and shell thickness of 20 nm in Ag). (b) Simulated near-field distribution patterns under each resonance wavelength (411, 440, 478, 540, 675 and 760 nm) resolved from (a). The simulation setup for the near-field extraction is schematically shown in the figure. As the spherical mode used in this work is symmetrical, both the TM modes and TE modes resonance can be simultaneously excited. The TM modes can be extracted by setting the field monitor paralleling to light polarization direction, while

the TE modes can be extracted by setting the field monitor perpendicular to the light polarization direction. The resonance pattern at longer wavelength shown in Figure 2a at about 1300 nm also has been simulated as shown in (b). From the extracted resonance patterns and charge distribution it can be concluded that the resonance in 411, 440, 478 and 540 nm should be classified as the series of plasmonic coupled WGM resonances. The TM modes (third order to fifth order as illustrated in the figure) with the local field exist on the exterior surface of cavity and a relatively higher quality (Q) factor exhibit as plasmonic modes, while the TE modes (first order to fourth order as illustrated in the figure) with light well confined within the ZnO layer present as series orders of pure dielectric cavity modes as shown in the figure. For longer wavelength (675, 760, 860 and 1300 nm), generally no cavity mode could exist in such small cavity due to its smaller size than the incident wavelength and Mie scattering from the particle would dominated in this region. According to the extracted near-field distribution at these wavelengths, the resonance looks more like as the multipole LSPR mode resonances with a broadband resonance peak as seen in the figure. So, the resonance modes in the Ag/ZnO HNS cavity can be clarified as two distinct regions: plasmonic coupled WGM resonance and the bare multipole LSPR resonance regions as illustrate in the figure.

S4. Hybridization model in the Ag/ZnO HNS cavity

In this work, the coupling effect between Ag shell layer and ZnO dielectric cavity can be explained by the hybridization model.[3] According to the plasmonic hybridization theory, plasmonic resonance in the Ag/ZnO HNS double shell structure can be considered as the hybridization between bare Ag HNS shell structure and ZnO HNS structure, as illustrated in Figure S4a below. After hybridization with ZnO hollow cavity, the specific plasmonic resonance band (ω_p) on the bare Ag HNS structure would split as two distinct resonance band in the same resonance order: low- (ω_{p-}, Symmetric) and high-energy (ω_{p+}, Antisymmetric) plasmon resonance bands. Here, the third order ($l = 3$) of plasmonic resonance clearly shows this hybridization phenomenon: a high-energy (ω_{p+} (3)) plasmon resonance band at 540 nm and low- (ω_{p-} (3)) plasmon resonance band at 760 nm emerged on Ag/ZnO HNS hybrid structure and they both belong to the third order of plasmonic resonance (as demonstrated in

Figure S3) except for the differences in charge distribution: antisymmetric and symmetric charge distribution characteristics as resolved in Figure S3, respectively. In fact, due to the multiple resonance modes (series order of plasmonic resonance modes and dielectric cavity modes) existed in the hybrid structure, it is still a challenge to clearly resolve all of hybridization process for each modes. The composite shell structure's parameters also need to be further optimized and controlled for the convenience to fully reveal the hybridization process on a specific resonance mode.
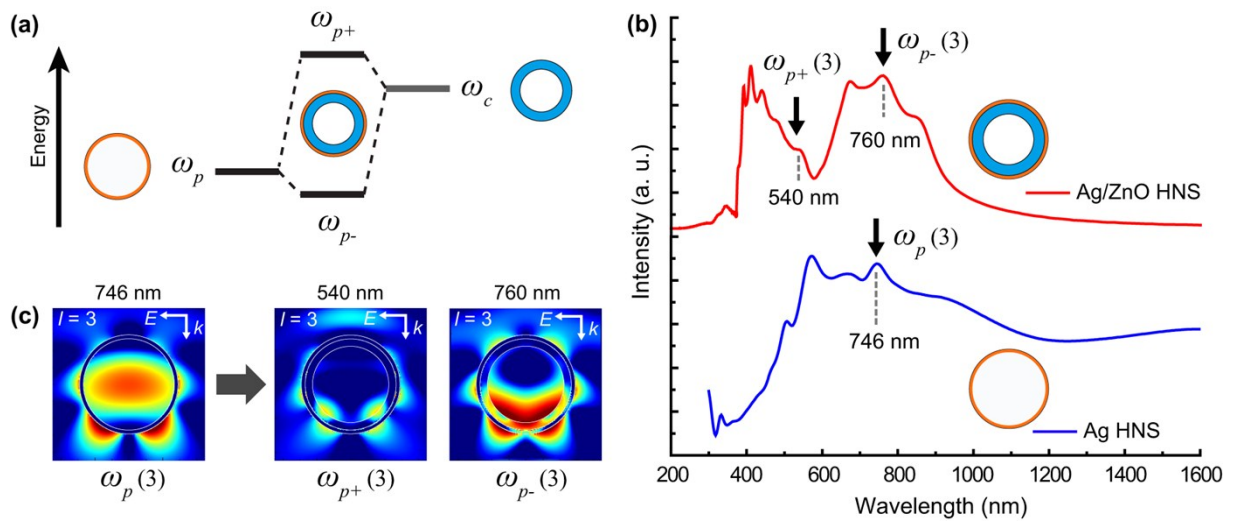
Figure S4. (a) Illustration of the plasmonic hybridization in Ag/ZnO HNS hybrid plasmonic cavity. (b) Comparison of the resonance and extinction spectra between a single Ag HNS and composite Ag/ZnO HNS structure. The resonance peak for the third order of plasmonic resonance (ω_p (3)) in the Ag HNS and the corresponding generated low- (ω_{p-} (3)) and high-energy (ω_{p+} (3)) plasmon resonance bands after coupling with the ZnO HNS cavity were marked with black arrows shown in the Figure. The local filed patterns for each resonance bands mentioned above were show in (c).

**S5. SERS performance on plasmonic nanocavity arrays with different core diameters**
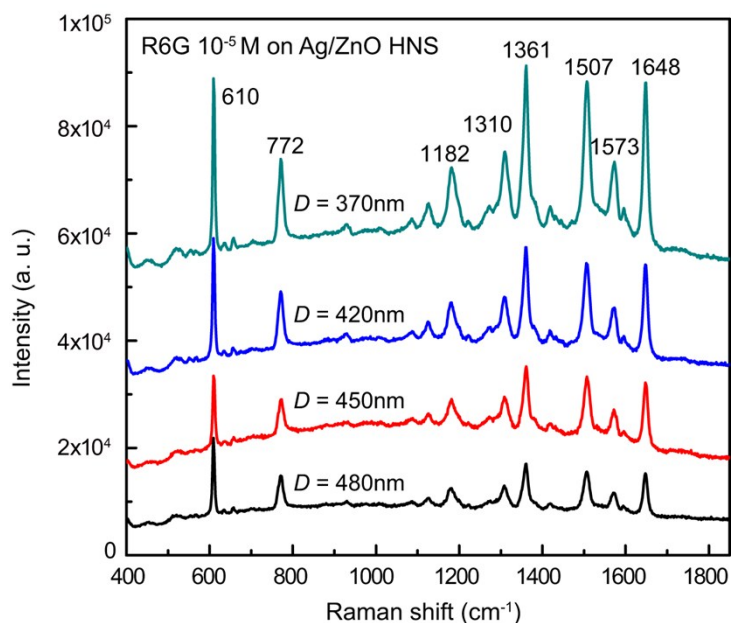
Figure S5. SERS characterization on the Ag/ZnO plasmonic cavity arrays substrates (a) with the core diameter of 480, 450, 420 and 370 nm respectively.

In order to fully utilize the intensive periodic hot spots produced in these plasmonic coupled metal/dielectric hollow nanocavities, corresponding SERS characterizations were performed using the low concentration R6G as the target analyte. Figure S4 shows the Raman spectra of R6G in the concentration of 10^{-5} M when dipped on the series of plasmonic nanocavity arrays with different core diameters of 480, 450, 420 and 370 nm. The results well agree with the FDTD simulation ones as discussed above that stronger Raman scattering intensity can be obtained for the samples with smaller core diameter and emerged gaps between cavities. The strongly localized near field on the surface of Ag/ZnO HNS arrays originated from the plasmonic coupled WGM resonance and the consequently generated hot spots due to the inter-coupling effect of the plasmonic cavities should be the main reason for this significantly enhanced Raman signals.

S6. SERS performance on ZnO HNS arrays and bare silicon substrate
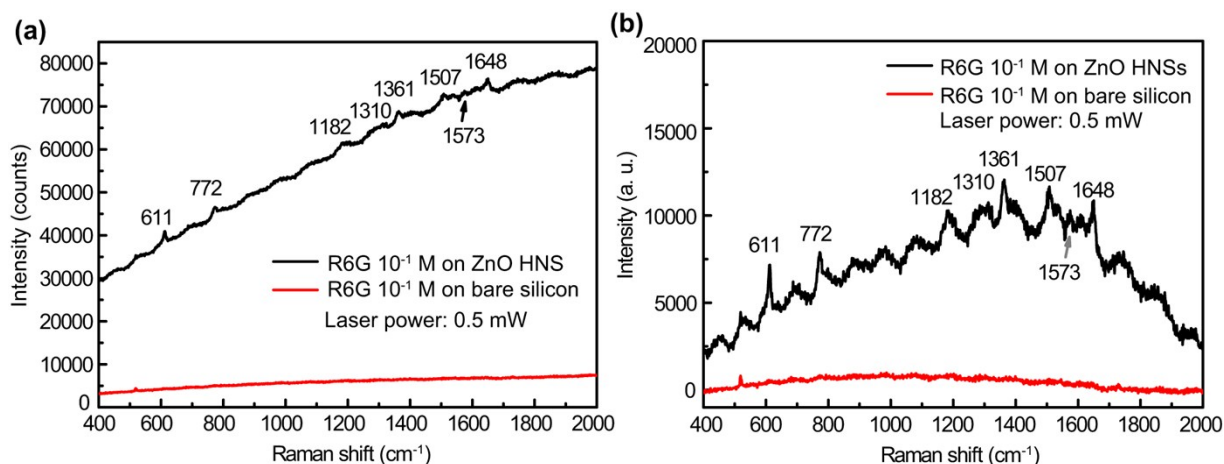
Figure S6. Raman spectra of R6G with a concentration of 10^{-1} M on ZnO HNS arrays and bare silicon substrate for a comparison (a) without and (b) with the baseline correction. It can be seen that strong fluorescence dominates the Raman spectra for both of the samples due to the absence of SPR property from metal. However, distinguished Raman signals, such as Raman bands 611, 772, 1182, 110, 1361, 1507, 1573 and 1648 cm^{-1} of R6G, still can be resolved from the ZnO HNS arrays sample, which should be originated from the enhanced local field induced by the WGM resonance in the ZnO HNS dielectric resonators.[4]

S7. SERS characteristics of PATP
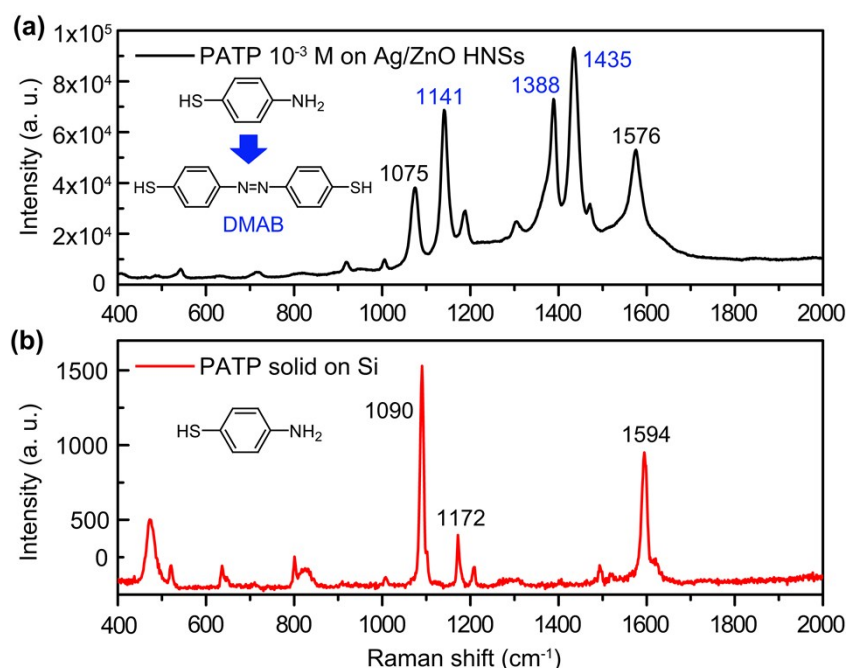
Figure S7. Raman spectra of (a) PATP solution (10^{-3} M) on Ag/ZnO HNS arrays and (b)

PATP solid materials on silicon substrate. Laser power is 5 mW in the Raman measurement. The newly emerged Raman peaks at 1141, 1388 and 1435 cm^{-1} indicate the typical SERS characteristics of according to the previous report.[5] The photo-induced charger transfer process from Ag to the Raman probe PATP in the Raman measurement causes the chemical transformation of PATP to 4,4′-dimercaptoazobenzene (DMAB), which makes the SERS signals of PATP on Ag/ZnO HNS arrays is much different from the Raman signals of PATP solid materials.

S8. Raman mapping characteristics
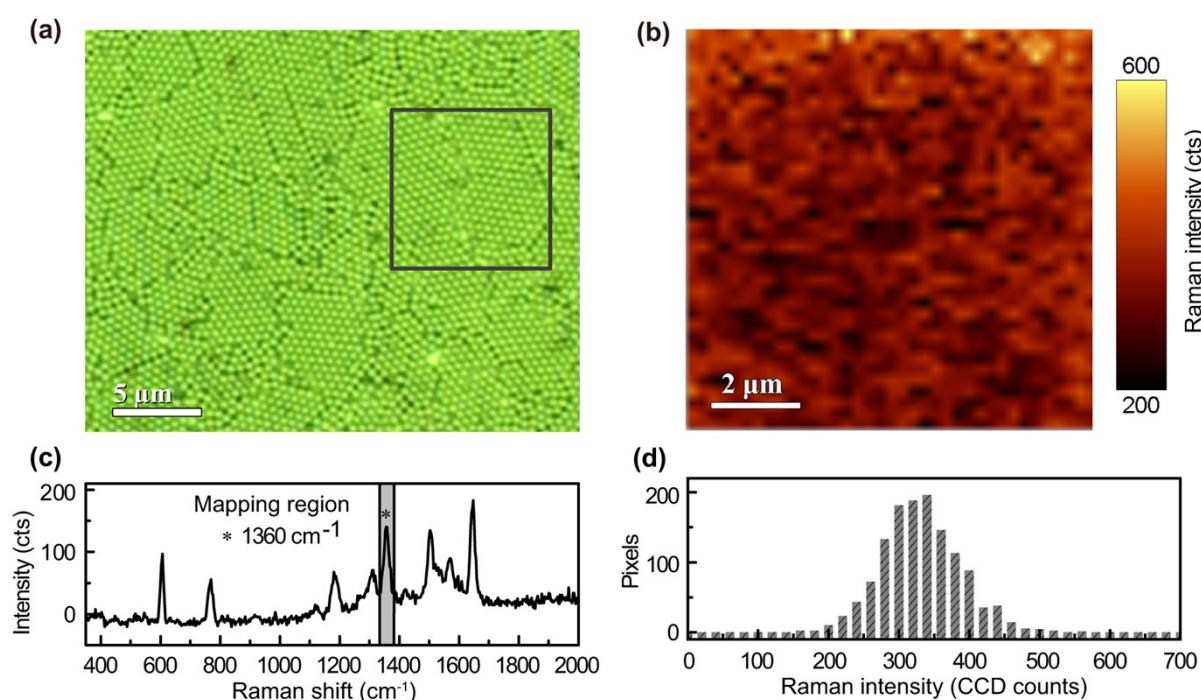
Figure S8. (a) Optical microscope image of as-fabricated large scale Ag/ZnO HNS arrays; (b) the corresponding Raman mapping image (9 μm × 9 μm) collected from the area marked by a box shown in (a). Each pixel in the confocal Raman mapping images represents integral Raman intensity near 1360 cm^{-1} (1320 cm^{-1} ~ 1400 cm^{-1}) in the interested area as shown in (c). Before integrating calculation, a background subtraction was performed in all spectra within the considered region. (d) Histogram of Raman intensities in the Raman mapping of (c).

References

1. F. Caruso, R. A. Caruso and H. Möhwald, *Science*, 1998, **282**, 1111-1114.

2. J. Yin, Y. Zang, C. Yue, Z. Wu, S. Wu, J. Li and Z. Wu, *J. Mater. Chem.*, 2012, **22**, 7902-7909.
3. E. Prodan, C. Radloff, N. J. Halas and P. Nordlander, *Science*, 2003, **302**, 419-422.
4. I. Alessandri, *J. Am. Chem. Soc.*, 2013, **135**, 5541-5544.
5. Y.-F. Huang, H.-P. Zhu, G.-K. Liu, D.-Y. Wu, B. Ren and Z.-Q. Tian, *J. Am. Chem. Soc.*, 2010, **132**, 9244-9246.